PLEASE CITE THIS ARTICLE AS DOI: 10.1063/5.0250478

# Enhancing Indoor Temperature Mapping: High-Resolution Insights through Deep Learning and Computational Fluid Dynamics

Filippos Sofos (Φίλιππος Σοφός),<sup>1, 2</sup> Dimitris Drikakis (Δημήτρης Δρικάκης),<sup>1, a)</sup> and Ioannis William Kokkinakis (Ιωάννης Κοκκινάκης)<sup>1</sup>

1) Institute for Advanced Modeling and Simulation, University of Nicosia, Nicosia CY-2417, Cyprus

This paper examines the temperature distribution in a closed, rectangular room equipped with an air conditioning system, employing a computational fluid dynamics model to simulate a virtual thermal camera that captures detailed temperature snapshots. A super-resolution framework enhances the post-processing of these results. Specifically, convolutional neural networks, trained on simulation data, are used to accurately model temperature fields' high-resolution spatial and temporal evolution. The model demonstrates strong performance by accurately reconstructing temperature profiles from low-resolution inputs obtained from filtering data obtained using high-resolution numerical simulations, with quantitative metrics indicating acceptable accuracy for resolutions reduced by up to 50 times. This effectively aligns with ground truth profiles under various conditions. These results underscore the super-resolution model's potential to transform environmental monitoring in smart buildings and complex structures by generating high-resolution thermal maps from low-resolution cameras or limited sensor input. This approach offers a fast, cost-effective, and reliable method for accurately modeling thermal dynamics within the turbulent flow environments of interior spaces.

### I. INTRODUCTION

Accurately estimating environmental conditions like temperature and humidity in indoor and outdoor spaces is crucial for effective building design and analysis. <sup>1,2</sup> In the context of global warming and urban heat islands, numerous strategies have been developed to enhance thermal environments. <sup>3</sup> Among these strategies, the installation of thermal cameras stands out as a practical solution. Thermal cameras can provide two-dimensional and even photo-realistic three-dimensional visualizations of room temperature. <sup>4</sup> By detecting infrared radiation, these cameras can monitor and capture temperature data, which can then be used to analyze the thermal properties of various structures. Variations in temperature values manifest as changes in pixel attributes such as color, brightness, and contrast within the thermal images. <sup>5</sup>

In a different methodological approach, computational fluid dynamics (CFD) simulations are extensively utilized to estimate airflow properties. The choice of method is contingent upon the desired level of accuracy. Commonly employed simulation techniques, ranging from lower to higher fidelity, include Reynolds Averaged Navier Stokes (RANS), Large Eddy Simulation (LES), and Direct Numerical Simulation (DNS). 6–10 However, achieving high-resolution fields can be computationally prohibitive and challenging practical applications. Typically, parameter fields are visualized as two-dimensional (2D) contours; hence, reducing computational costs is imperative. Integrating deep learning (DL) techniques into these simulations offers a promising solution. 1

To ensure thermal comfort in contemporary building applications, several AI-driven predictive methods have been introduced, including Artificial Neural Networks (ANNs), Support Vector Machines (SVMs), Random Forests (RF), and various

tree-based variants. <sup>12–14</sup> While effective for property prediction tasks, these methods often struggle with large-scale data applications like imaging or complex problem-solving. Here, DL algorithms excel, demonstrating impressive performance on intricate tasks. <sup>15</sup>

Apart from surrogate models that follow an end-to-end approach, efforts to integrate CFD simulations with Machine Learning (ML) and DL methods have been reported <sup>16</sup>, trying to minimize the inherent computational load. For instance, "CFDNet", a physical simulation and deep learning coupled framework, combines CFD with DL to boost the convergence speed of RANS, achieving acceleration up to 7.4 times in various flow cases. <sup>17</sup> The gene-expression programming (GEP) method has also been combined with RANS for turbulent flow investigation. <sup>18</sup> Bode and Göbbert <sup>19</sup> propose a DL-assisted large-eddy simulation (LES) framework that exploits DNS data both to train the DL network and extract the ensemble statistics. In Kashefi, Rempe, and Guibas <sup>20</sup>, CFD grid information input enters a DL network, and flow results are obtained faster and with high accuracy.

The analysis of turbulent flow fields characterized by dynamic properties such as velocity, temperature, vorticity, and pressure, as well as 2D and three-dimensional (3D) image reconstruction from sparse data, presents a viable option. This process involves correlating image pixel values with calculated properties via post-processing analysis. <sup>21,22</sup> Several DL architectures have been developed to tackle such challenges, utilizing layer-wise approaches to synthesize nonlinear functions. <sup>23–26</sup>

A particularly relevant DL method for image reconstruction is the super-resolution (SR). <sup>27,28</sup> SR focuses on training networks with high-resolution (HR) and low-resolution (LR) pairs of 2D data, learning their mapping for application in scenarios lacking HR data. However, transitioning from HR to LR images can introduce degradation issues due to the loss of high-frequency features such as sharp edges and textures. <sup>29</sup>

Low-frequency areas, like large uniform backgrounds, generally remain unaffected. In practice, LR fields can result from

<sup>2)</sup> Condensed Matter Physics Laboratory, Department of Physics, University of Thessaly, Lamia 35100, Greece

a)Electronic mail: Author to whom correspondence should be addressed: drikakis.d@unic.ac.cy

PLEASE CITE THIS ARTICLE AS DOI: 10.1063/5.0250478

Preprint 2

low-resolution sensor measurements, such as those from cameras or pressure sensors, where high-resolution alternatives are impractical due to financial or technological constraints. Moreover, low-grid simulations, which are computationally less demanding, can also yield LR results. Employing post-processing reconstruction methods to upscale LR images is therefore critical, aiding in replicating original quality features as closely as possible to the ground truth. 30–32

In SR applications, monitoring information flow from sparse sensor networks involves mapping data to a computational grid, typically a 2D grid resembling a low-resolution image. The LR image is reconstructed to yield an HR field without additional sensors. Given the ultra-low resolution of field images, sensor placement becomes paramount<sup>33</sup>. Despite the potential challenges such as image noise<sup>34</sup>, computational solutions often offer advantages over experimental ones, circumventing technical issues like camera shake, lens defocus, and atmospheric interference<sup>35</sup>.

High-dimensional data handling presents challenges, including hardware limitations, memory demands, and slow execution times. Standard DL architectures, like feed-forward neural networks, are not well-suited for these applications<sup>36</sup>. Instead, more efficient architectures such as convolutional neural networks (CNNs) are employed.<sup>37–39</sup> CNNs process 2D or 3D images through convolution operations, producing outputs that retain key image features while minimizing data volume.<sup>40</sup> Key considerations for CNN-based SR applications include (i) the depth of internal layers<sup>41</sup>, (ii) the convolution and deconvolution pipeline, often forming a U-shaped network<sup>42</sup>, (iii) the selection of pooling layers (max or average)<sup>39</sup>, and (iv) the inclusion of residual/skip connections to transfer high-fidelity information between input and output layers.<sup>43</sup>

The current baseline setup involves an indoor environment with temperature control managed by an air-conditioning (A/C) system. CFD simulations model the flow of conditioned air, and a succession of 2D iso-surface temperature field images are extracted for subsequent analysis. A DL architecture is trained on these data sets to map sparse input onto a high-resolution grid. <sup>44,45</sup> This method enables a camera device to provide a complete temperature map of the space while eliminating additional sensor devices. The proposed approach offers a pragmatic and cost-effective solution for simulating desired flow properties within buildings.

Subsequent sections detail the CFD simulation methodology and the processes for obtaining accurate temperature contours. They also provide a comprehensive explanation of the SR architecture and reconstruction framework. Results from reconstructed temperature profiles are presented, along with an error analysis to evaluate the method's efficacy. The study summarizes key findings and suggests future research directions for integrating computational models with real-world devices.

### II. FLUID FLOW AND DEEP LEARNING METHODS

### A. Fluid Flow Model

The three-dimensional Navier-Stokes (NS) equations for a Newtonian viscous air mixture are considered. For a finite control volume, V, the multi-component NS equations can be written in the fully-conservative and Cartesian co-ordinates form as follows:  $^{46}$ 

$$\frac{\partial}{\partial t} \iiint_{V} \rho \, dV = \iint_{A} -\rho \mathbf{u} \cdot \hat{\mathbf{n}} dA, \tag{1}$$

$$\frac{\partial}{\partial t} \iiint_{V} \rho \mathbf{u} \, d\mathbf{V} = \oiint_{A} (-\rho \, \mathbf{u} \otimes \mathbf{u} - p \, \mathbf{I} + \tau) \cdot \hat{\mathbf{n}} d\mathbf{A} 
+ \iiint_{A} \rho \mathbf{f}_{b} \, d\mathbf{V},$$
(2)

$$\frac{\partial}{\partial t} \iiint_{V} \rho e_{t} \, dV = \iint_{A} (-\rho h_{t} \mathbf{u} + \mathbf{u} \cdot \boldsymbol{\tau} - \mathbf{q_{c}} - \mathbf{q_{d}}) \cdot \hat{\mathbf{n}} dA 
+ \iiint_{U} \rho \left( \mathbf{f}_{b} \cdot \mathbf{u} + \dot{h} \right) dV,$$
(3)

$$\frac{\partial}{\partial t} \iiint\limits_{V} \rho w_{j} \, dV = \iint\limits_{A} (-\rho w_{j} \mathbf{u} + \mathbf{J}_{j}) \cdot \hat{\mathbf{n}} dA 
+ \iiint\limits_{A} \rho \dot{w}_{j} \, dV,$$
(4)

where  $\rho$  is the mixture density;  $\mathbf{u}$  is the velocity vector; p is the static pressure;  $\hat{\mathbf{n}}$  is the outward pointing unit normal of a surface element dA of the closed finite control volume dV;  $\mathbf{f}_b$  is an external body force;  $h_t = e_t + p/\rho$  is the total specific enthalpy (per unit mass);  $e_t = e + \mathbf{u} \cdot \mathbf{u}/2$  is the total specific energy;  $e = c_v T$  is the specific internal energy;  $w_j$  is the massfraction of the j-th species. We denote T the temperature,  $c_v$  the specific heat capacity at constant volume, and  $\gamma = c_p/c_v$  the heat capacity ratio where  $c_p$  and  $c_v$  are the specific heat capacity at constant pressure and volume, respectively.

For a Newtonian fluid, the shear stress tensor is given by:

$$\tau = \lambda \left( \nabla \cdot \mathbf{u} \right) \mathbf{I} + \mu \left[ \nabla \otimes \mathbf{u} + \left( \nabla \otimes \mathbf{u} \right)^T \right], \tag{5}$$

where I is the identity tensor,  $\lambda = -2\mu/3$  is the second viscosity coefficient given by the Stokes hypothesis, and  $\mu$  is the dynamic viscosity. The heat flux is calculated according to Fourier's Law of heat conduction, i.e.,  $\mathbf{q_c} = -\kappa \nabla T$ , where  $\kappa = c_p \mu/Pr$  is the thermal conductivity and Pr is the Prandtl number. The species diffusional fluxes are commonly computed via the Fickian (gradient) diffusion approximation, i.e.,  $\mathbf{J_j} = \rho D_j \nabla w_j$ , where  $D_j = \mu_j/(\rho Sc_j)$  is the  $j^{th}$  species mass

PLEASE CITE THIS ARTICLE AS DOI: 10.1063/5.0250478

diffusivity and Sc is the Schmidt number. The energy equation includes the inter-diffusional enthalpy flux arising from the species mixing<sup>47</sup>, i.e.,  $\mathbf{q_d} = -\sum_{i=1}^{N_{sp}} h_i \mathbf{J}_i$ , where the enthalpy of each *i*-th species is defined by  $h_i = e_i + p_i/\rho_i$ . No heat or mass sources, i.e.,  $(\dot{h})$  and  $(\dot{y})$ , are considered in the present study.

The above formulation of the governing equations represents the fully conservative 4-equation model of Allaire, Clerc, and Kokh 46. Equation (1) governs the evolution of the mixture density while Eq. (4) is used for the density of the first component ( $\rho_1 = \rho w_1$ ). The density of the second component is then obtained from the mixture relation  $\rho = \rho w_1 + \rho w_2$ .

Equations 1-4 are solved in dimensionless form. The reference units used are [L]ength =  $L_{ref}$ , [M]ass =  $L_{ref}^3 \rho_{ref}$ , [T]ime =  $L_{\text{ref}}/u_{\text{ref}}$ , and [t]emperature =  $T_{\text{ref}}$ . Suppose superscript {\*} designates a variable in units. In that case, the dimensionless variable is obtained by dividing by the appropriate reference unit(s), e.g.,  $\rho = \rho^*/\rho_{\rm ref}, \ u = u^*/u_{\rm ref},$  $p = p^* / (\rho_{\text{ref}} u_{\text{ref}}^2)$ ,  $T = T^* / T_{\text{ref}}$ , and all remaining variables follow suit. Note that in the case the viscosity is taken as a constant, it is non-dimensionalized according to  $\mu = \mu^*/\mu_{ref}$ , or otherwise  $\mu = 1/\text{Re}_{\text{ref}}$  where  $\text{Re}_{\text{ref}} = \rho_{\text{ref}} u_{\text{ref}} L_{\text{ref}} / \mu^*$ . However, the present calculations employ Sutherland's Law to calculate the dynamic viscosity.

## B. CFD Method

The simulations used the CFD code CNS3D (Compressible Navier-Stokes 3D)<sup>48-50</sup>, which employs a Godunov-type method for advective terms, solved via the Riemann problem. CNS3D supports Revnolds-Averaged Navier-Stokes (RANS), Implicit Large Eddy Simulation (ILES), and Direct Numerical Simulation (DNS).<sup>50–53</sup> In this paper, we have used the ILES framework.54,55 ILES in CNS3D has been extensively validated over several cases published in the above literature.

Regarding the numerical methods in CNS3D, the "Harten-Lax-van Leer-contact HLLC" Riemann solver<sup>58</sup> is used. The reconstruction of the flow variables at the cell faces is performed using a modified 11th-order weighted essentially non-oscillatory (WENO) scheme<sup>50</sup> that handles low-Mach number issues better than the Monotonic Upstream-centered Scheme for Conservation Laws (MUSCL) schemes<sup>57,59</sup> when low-Mach corrections are used.<sup>60</sup> Higher-order methods provide better accuracy<sup>57,59</sup> and scale well over large systems. Phase variables are reconstructed following the papers of 61, to prevent spurious oscillations at fluid interfaces. Viscous terms use a fourth-order central scheme<sup>48,51</sup>, advanced in time by a five-stage Runge-Kutta method. 50 More information on CNS3D and its validation can be found in 50,51 and other references therein.

### C. Domain setup & boundary conditions

The temperature of a closed rectangular indoor region, with dimensions of  $6.0 \times 2.4 \times 2.8$  meters (length  $\times$  height  $\times$ width), is controlled by an A/C unit. The unit is placed at the center of the ceiling and comprises a square outlet (48 cm<sup>2</sup>) and four rectangular inlets ( $48 \times 4 \text{ cm}^2 \text{ each}$ ), "pushing" cold air at 18 °C and a 45°degrees angle relative to the centerline. Figure 1 illustrates the flowfield that develops in the rectangular room - about 1 minute after the A/C unit was turned on. Based on the A/C inlet height (4 cm) and inlet velocity (4 m/s), the inlet Reynolds number is  $Re_j \simeq 11,000$ .

The initial room temperature is 25 °C with a 60% relative humidity. The simulation considers a binary multicomponent flow, such that the mass-fractions of the binary (two-component) mixture obey  $w_1 + w_2 = 1$ , where the values of w<sub>1</sub> and w<sub>2</sub> depend on the air properties, i.e., the relative humidity and temperature. The first component  $(w_1)$  is dry air (0% moisture) with an adiabatic index of  $\gamma_1 = 7/5$  and molar mass of  $\mathcal{M}_1 = 28.964$  kg/kmol. The second component  $(w_2)$ is water vapor with an adiabatic index of  $\gamma_2 = 4/3$  and molar mass of  $M_2 = 18.015$  kg/kmol. The relative humidity difference between the room's ambient air and the cooler air from the A/C unit generally arises from the condensation within the A/C unit. This results in a variation in the mass fractions between the two separate air streams.

The velocity is initially assumed to be equal to zero everywhere in the room. The pressure varies in the normal (y) direction due to gravity, i.e.,

$$p(y) = p_0 + \rho g_y y \,, \tag{6}$$

where the Earth's gravitational acceleration is taken as  $g_v =$ -9.81 m/s<sup>2</sup>. The internal energy,  $e_i$  is calculated according

$$e_i = \frac{p_1 + p_2}{\gamma - 1} \;, \tag{7}$$

where  $p_1$  is the partial pressure of the dry air component in the room and  $p_2$  is the water vapor partial pressure. The former is obtained according to  $p_1 = p_0 - p_2$ , where  $p_0$  is the stagnation pressure at ground/sea level, i.e.,  $p_0 = 101,325$  Pa. The water vapor pressure is calculated according to  $p_2 = x_2 p_0$ , where the molar-fraction is  $x_2 = w_2(\mathcal{M}/\mathcal{M}_2)$ , and the total molar mass of a miscible mixture is obtained according to:

$$\mathcal{M} = \frac{1}{\sum_{i} (w_i / \mathcal{M}_i)} \tag{8}$$

where  $w_i$  is the mass-fraction of the *i*-th component. The initial air mixture density,  $\rho$ , solved by Eq. (1) is taken to be constant and is calculated based on the prescribed relative humidity, i.e., the fraction of water vapour and dry air:

$$\rho = \rho_1 + \rho_2 = \rho w_1 + \rho w_2 , \qquad (9)$$

where the components' partial density can be obtained from  $\rho_i = p_i / (R_s^i T_0)$ ;  $R_s^i$  is the specific gas constant of the *i*-th component and  $T_0$  is the initial (stagnation) room temperature.

We have used a block-structured hexahedral orthogonal Cartesian mesh. The computational cells have an edge length of 2 cm ( $\Delta x^+ \simeq 700$ ), resulting in a mesh resolution of  $300 \times 120 \times 140$ , giving a total of 5,040,000 cells; the cell size is the same in all directions:  $\Delta x = \Delta y = \Delta z = 2$  cm. We

PLEASE CITE THIS ARTICLE AS DOI: 10.1063/5.0250478

Preprint

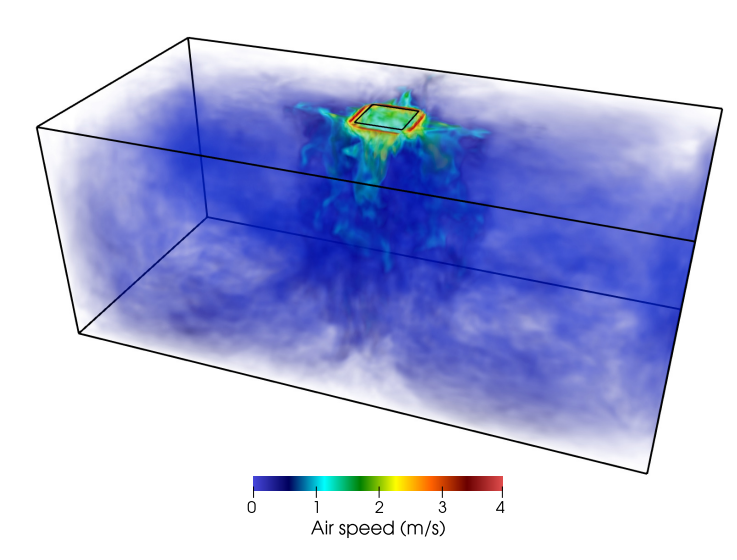


FIG. 1. Illustration of the flow field in the rectangular room considered. A/C unit is located at the centre of the ceiling.

have performed numerical experiments with coarser meshes containing hexahedral cells with double the edge length (i.e., 4 and 8 cm) and a finer mesh with an edge length of 1 cm. For 90 seconds of actual flow time, the results on the finer mesh exhibited less than < 1.3% difference compared to the elected mesh (edge length of 2 cm). ILES encompasses a wide variety of approaches that rely upon the dissipation of the numerical scheme to model the small unresolved (sub-grid) scales to dissipate the large, resolved turbulence scales. Comparisons of implicit and explicit modeling using the same numerical method and grid show that the implicit method is much less dissipative. 63 The present setup assumes the flow from the jet inlets to be laminar and, thus, the breakdown of the free-shear (mixing) layer(s) to occur more gradually and at larger scales. The fine-scale turbulence formed subsequently is not attempted to be directly resolved as the computational cost would otherwise become exceedingly high. Moreover, the smaller (unresolved) scales gradually weaken and have an increasingly smaller effect on the flow and the image data extracted and used. Note that the purpose of the present study is not to analyze the turbulence properties of the free shear layer(s), but rather to test the suitability of machine learning to complex evolving flows such as the one the present study considers.

# D. Super Resolution Deep Learning

Convolutional neural networks (CNNs) have been extensively applied to imaging tasks, including SR applications. In these architectures, input 2D data is processed through network layers, where spatial features are extracted and represented within filters. Although the CFD approach was simulated in 3D to ensure an accurate and realistic representation of the flow physics, the DL network layers operate in 2D to balance computational efficiency with predictive accuracy. The basic function of such layers is the convolution operation, where image regions are filtered and coded in batches and passed to the next layer. The deconvolution operation performs the decoding part and re-creates the input image. To ensure normalization between layers and increase performance. average and max pooling layers and flatten, concatenate, and batch normalization layers are employed.3

In fluid mechanics, CNNs are widely incorporated due to their ability to handle sparse representations, in contrast to ANNs, and achieve better performance in significantly lower computational times and memory loads.<sup>64</sup> A notable deep learning framework for SR upscaling is the Deep Learning Flow Image (DELFI) architecture, which has been successfully used for temperature field reconstruction. This architecture is accurate and relatively straightforward, incorporating CNNs and residual connections.

DELFI processes a set of LR images alongside the corresponding HR images, which serve as ground truth data.6 Flow images are pre-processed before entering the network pipeline to ensure the correct dimensions. They are linearly interpolated to the GT dimensions, making comparison and processing inside the CNN layers possible. Next, they pass through successive CNN layers, which generate multichannel feature maps. 66 The first CNN layer applies 64 convolutional filters, each designed to detect distinct image features across various frequency ranges. These filters are implemented using a 3 × 3 convolutional kernel, which scans the input image regions sequentially, followed by the Rectified Linear Unit

PLEASE CITE THIS ARTICLE AS DOI: 10.1063/5.0250478

Preprint

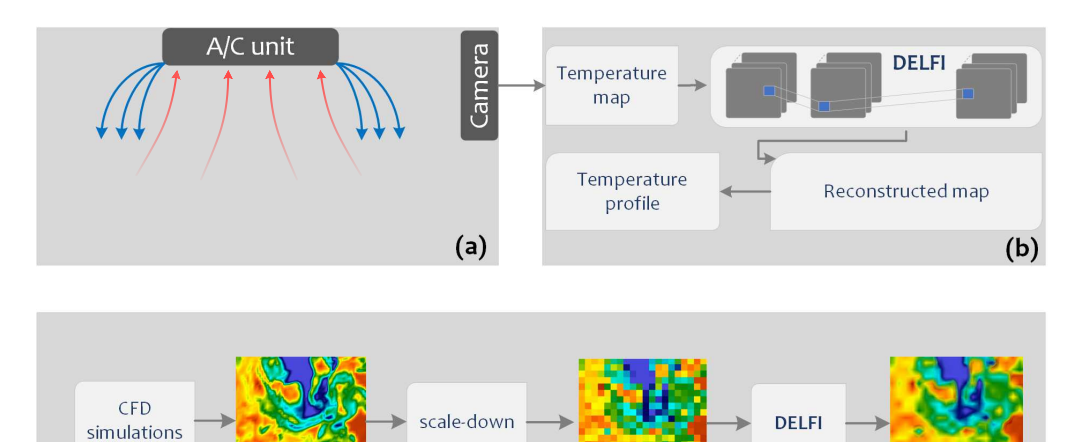


FIG. 2. (a) The process of taking images from a thermal camera, (b) the reconstruction architecture exploited based on DELFI, and (c) the training process of DELFI with simulation images.

(ReLU) activation layer. The second CNN layer also employs 64 filters and ReLU activation. During the deconvolution operation, residual information from the input image is incorporated to recover the possible loss, followed by a deconvolutional layer. The final layer aggregates the filters to produce a reconstructed output image with the same dimension as the input images. This is achieved through proper calibration of the stride and padding parameters.

This fast and easy-to-implement architecture has been tested on various turbulent pressure and velocity fields and has proven efficient, even when executed on standard hardware <sup>21,41</sup>. This work uses DELFI to reconstruct and upscale a sparse temperature field to achieve high-resolution detail. Additionally, to better understand temperature variations across the room's height, temperature profiles are extracted from various regions beneath the A/C unit, where the airflow is more rapid and turbulent, leading to finer structural details.

Figure 2 illustrates the flow diagram of the reconstruction process. Initially, two-dimensional temperature contours are captured using a high-resolution thermal camera within the room (see Fig. 2a). These 2D images serve as input to the DELFI pipeline, from which precise temperature profiles are extracted (Fig. 2b).

The training of the DELFI model is crucial, especially in this context where the primary challenge is accurately reconstructing fine and small-scale turbulent structures. To tackle this, flowfield data generated from high-resolution computational fluid dynamics (CFD) simulations (detailed in Section II C) are utilized to construct a comprehensive training dataset. A scaling factor, s, is used to reduce the resolution of

the high-resolution output temperature fields. Table I presents the dimensions of the scaled images used for training.

(c)

TABLE I. Input image resolution at various scales, where *s*=1 is the ground truth image.

| S            | 1          | 10       | 20       | 50      |
|--------------|------------|----------|----------|---------|
| $W \times H$ | 2240 × 896 | 224 × 89 | 112 × 44 | 44 × 17 |

Starting from the high-resolution  $(W \times H \times 3) = (2240 \times 896 \times 3)$  coloured image, with three channels (Red, Green, and Blue - RGB), the scaling-down factor reaches as low as s=50, to emulate the cases when an ultra-low resolution field might enter the DELFI pipeline. The scaled-down low-resolution counterparts are fed to DELFI to train the model effectively, and the reconstructed output is compared to the original high-resolution image. Through this process, DELFI "learns" the mapping between a low- and a high-resolution field so that it can apply it later in similar cases, for example, when the input is just a low-resolution field from a real camera. The CFD temperature field dataset contains 273 images, 193 of which are employed for training, 40 for validation and 40 for testing.

## III. RESULTS AND DISCUSSION

For presentation purposes, three-time instances are selected to extract the temperature (T) profiles across the room near the

PLEASE CITE THIS ARTICLE AS DOI: 10.1063/5.0250478

Preprint 6

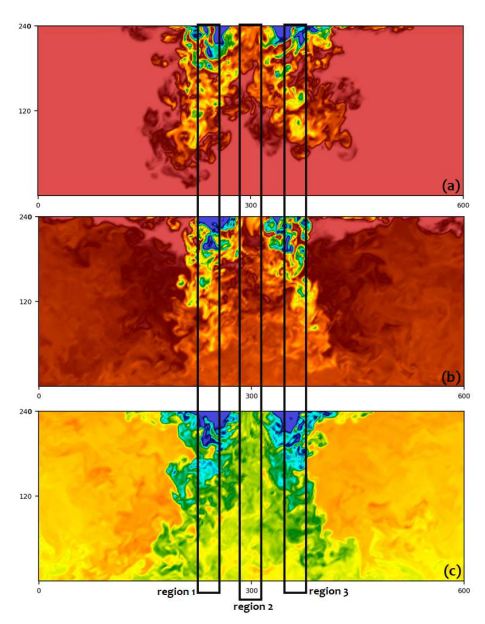


FIG. 3. Image regions considered for extracting the temperature profiles, under the left exit of the A/C unit, at the centre of the room, and under the right exit of the A/C unit (black rectangles) at various simulation times: (a) near the beginning of air-flow, (b) in the middle, and (c) at the end of the simulation. Dimensions shown are in [cm].

simulation's beginning, middle, and end. Figure 3 illustrates three example contour plots corresponding to these instances. Additionally, three specific regions are chosen for temperature profile extraction: the first is located at the left exit of the A/C unit (region 1), the second is in the center of the room (region 2), and the third is at the right exit of the A/C unit (region 3). These regions are characterized by turbulent airflow, thus presenting the greatest challenges for image reconstruction.

### A. Temperature profiles

From an average room temperature of 25 °C, cold air at 18 °C is expelled from the A/C unit, rapidly generating a highly turbulent flow. In each contour image, pixels represent temperature values. Let  $T_i$  represent the temperature in the i-th pixel across the room height, where  $i=1,2,3,\ldots,n$  and n is the total number of pixels in the y-axis. The temperature profile is defined by:

$$T_i = \frac{1}{N_i} \sum_{i=1}^{N_i} T_{ij}.$$
 (10)

where  $T_i$  is the time-averaged temperature in the i-th pixel bin within a time-frame of  $N_i$  measurements, and  $T_{ij}$  is the tem-

perature measurement j for each time instance in the i-th pixel bin.

For a reconstructed profile, the number of available pixels across the *y*-axis (the image height, H) varies according to the image resolution given by the camera (Table 1). Remarkably, the proposed SR model can help reconstruct a temperature profile even from a 17-pixel height, low-resolution image (s = 50).

Figure 4a displays the temperature profiles for s = 1 (i.e., the ground truth, GT), the SR-extracted field for s = 10, and the respective low resolution (LR) field, at region 1, near the start of the simulation. At this stage, only the temperature near the room's ceiling is expected to be affected by the colder air emitted from the A/C unit. The SR profile aligns perfectly with the GT profile, and is significantly better than the LR profile, which deviates from the GT, especially near the ceiling where high-temperature variations are observed. When a lower resolution image is processed (e.g., for s=20 in Fig. 4b), the DELFI reconstruction achieves fine-scale results across the room; this applies except for the highly turbulent region in front of the left A/C exit, where some inaccuracies are evident. These are attributed to the large temperature differences in this region, making it hard for the SR model to adjust effectively. These inaccuracies are more pronounced in the LR counterpart, as seen from the profile. Nevertheless, the overall reconstruction accuracy remains fine even when the input image resolution drops by s = 50, as shown in Fig. 4c, where the proposed model output qualitatively follows the GT temperature profile. This also remains the case for region 2 (Figs. 4d-f) and 3 (Figs. 4g-i).

Near the half-time of the simulation, the cold air spreads across the room. Airstreams can be seen chaotically reflecting off the walls, and the temperature fields observed are now highly turbulent. Figure 5 presents the obtained temperature profiles for regions 1, 2 and 3. In this image set, temperature changes are even more sudden and abrupt. Nevertheless, the SR reconstructed profiles remain close to the ground truth profiles for s = 10 - 20, and marginally for s = 50. In all cases, they are closer to the GT than the respective LR profiles.

Finally, near the end of the simulated period, at region 1 (Fig. 6a-c), an average temperature of  $T=18\,^{\circ}\mathrm{C}$  has been stabilized from the ceiling to a 100 cm region. At the same time, it linearly increases again as we approach the floor, reaching  $T=30\,^{\circ}\mathrm{C}$ . In region 2 (Fig. 6d-f), there is a linear increase from 24 to 32  $^{\circ}\mathrm{C}$ , while, in the right air outlet of the A/C unit, an average temperature of  $T=22\,^{\circ}\mathrm{C}$  is observed from the ceiling down to a 150 cm region. It abruptly increases to  $T=32\,^{\circ}\mathrm{C}$  towards the floor. The SR profiles follow the GT behavior for s=10-20, slightly deviate for s=50, and, compared to the LR profiles, they seem to achieve good reconstruction results.

### B. Accuracy metrics

A quantitative analysis follows, for which accuracy metrics are calculated to assess the reconstruction ability of the proposed SR model. The mean absolute error (MAE), the

PLEASE CITE THIS ARTICLE AS DOI: 10.1063/5.0250478

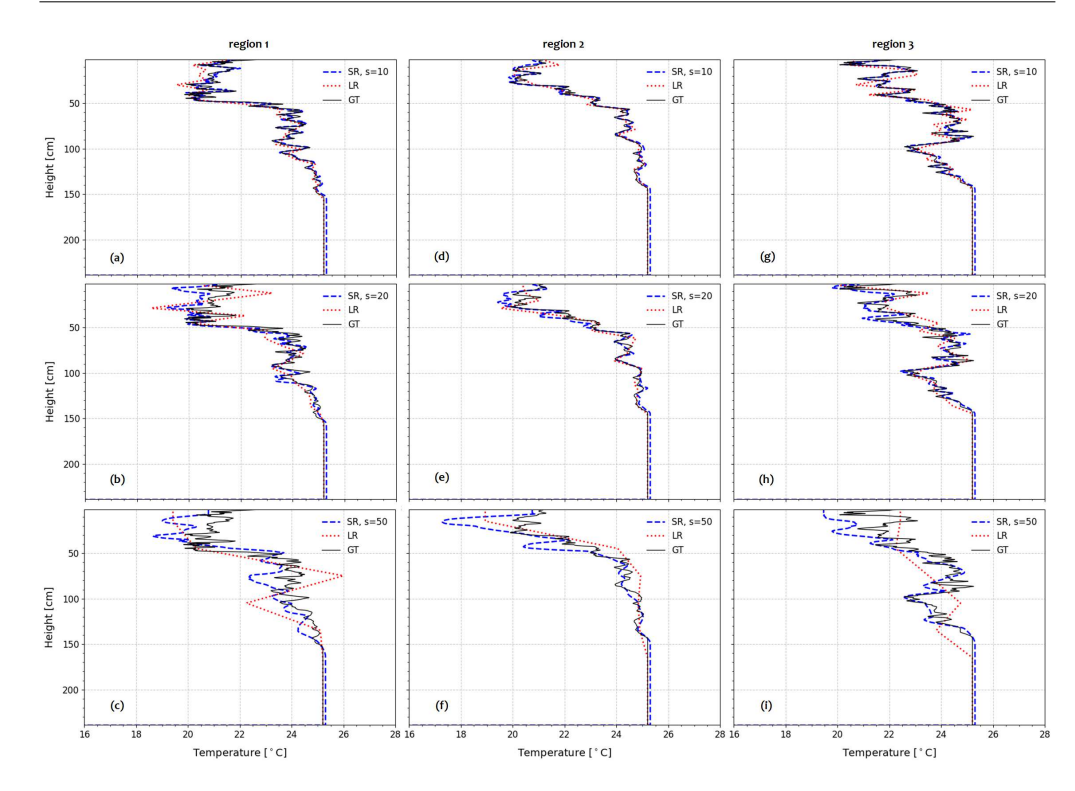


FIG. 4. Temperature profiles taken near the beginning of the simulation. The SR-extracted are compared to the ground truth (GT) profiles for region 1 and resolution (a) s=10, (b) s=20, and (c) s=50, for region 2 and (d) s=10, (e) s=20, and (f) s=50, for region 3 and (g) s=10, (h) s=20, and (i) s=50. Red dotted lines are the respective LR inputs used for training.

root mean square error (RMSE), the coefficient of determination (R2), and the mean absolute percentage error (MAPE) are given for a wide range of down-scaled images, s = 5 - 100.

The MAE is calculated as the average absolute difference between the GT values  $(GT_i)$  and the reconstructed values  $(SR_i)$ :

$$MAE = \frac{1}{n} \sum_{i=1}^{n} |GT_i - SR_i|.$$
 (11)

The RMSE measures the square root of the average of the squared differences between the GT values  $(GT_i)$  and the reconstructed values  $(SR_i)$ :

RMSE = 
$$\sqrt{\frac{1}{n} \sum_{i=1}^{n} (GT_i - SR_i)^2}$$
. (12)

The  $\mathbb{R}^2$  quantifies the proportion of the variance in the dependent variable that is predictable from the independent variable

ables. It is calculated as:

$$R^{2} = 1 - \frac{\sum_{i=1}^{n} (GT_{i} - SR_{i})^{2}}{\sum_{i=1}^{n} (GT_{i} - \bar{S}R)^{2}},$$
(13)

where SR is the mean of the reconstructed values  $(SR_i)$ .

The MAPE measures the percentage difference between the  $GT_i$  and the  $SR_i$  values, relative to the  $GT_i$ . It is calculated as the mean of the absolute percentage of errors:

$$MAPE = \frac{1}{n} \sum_{i=1}^{n} \left| \frac{GT_i - SR_i}{GT_i} \right| \times 100$$
 (14)

In addition, the  $L_2$ -norm and the  $L_\infty$ -norm are also incorporated to provide further insight into the model performance <sup>67</sup>. The  $L_2$ -norm measures the magnitude of the overall error by computing the Euclidean distance between the ground truth (GT) and the reconstructed profiles (SR), as:

$$L_2 = \sqrt{\sum_{i=1}^{n} (GT_i - SR_i)^2}.$$
 (15)

PLEASE CITE THIS ARTICLE AS DOI: 10.1063/5.0250478

Preprint 8

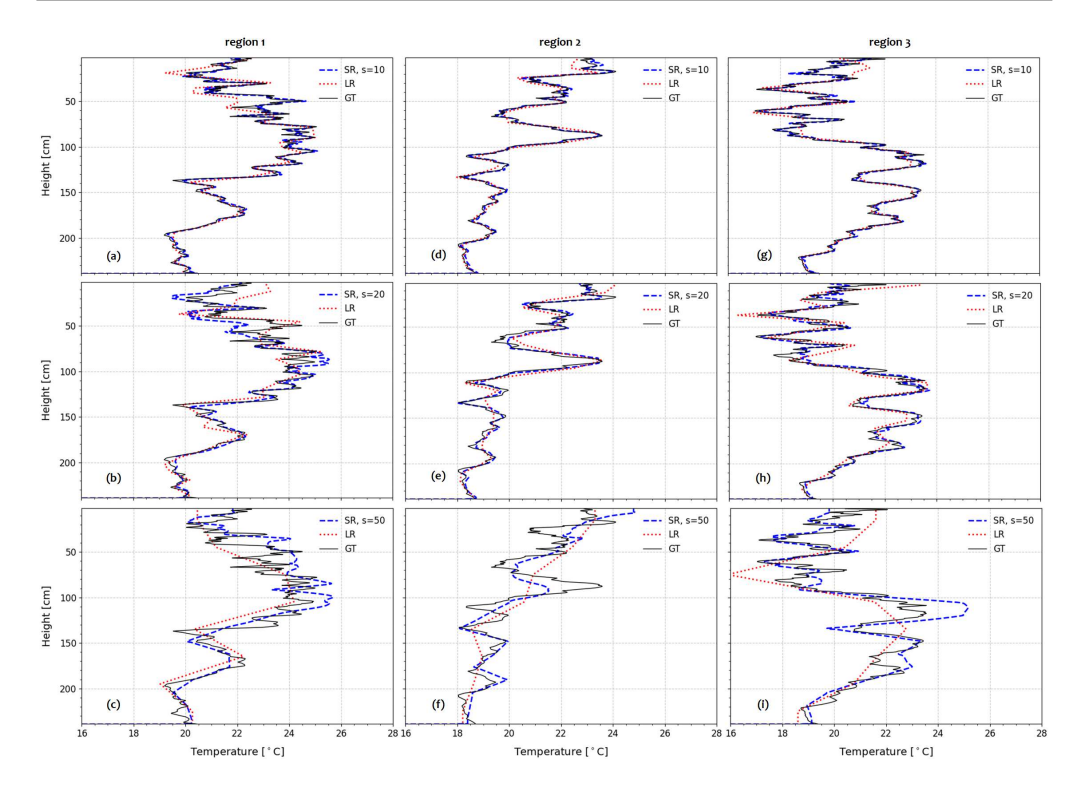


FIG. 5. Temperature profiles taken near the half-time of the simulation. The SR-extracted are compared to the ground truth (GT) profiles for region 1 and resolution (a) s=10, (b) s=20, and (c) s=50, for region 2 and (d) s=10, (e) s=20, and (f) s=50, for region 3 and (g) s=10, (h) s=20, and (i) s=50. Red dotted lines are the respective LR inputs used for training.

This metric emphasizes larger errors due to its quadratic nature, similar to RMSE, which makes it particularly useful for evaluating the overall accuracy of the reconstruction.

The  $L_{\infty}$ -norm, on the other hand, quantifies the maximum absolute deviation between the ground truth and the SRreconstructed values:

$$L_{\infty} = \max_{i \in \{1, 2, \dots, n\}} |GT_i - SR_i|. \tag{16}$$

By highlighting the largest error, the  $L_{\infty}$ -norm is instrumental in identifying worst-case discrepancies, which is crucial in applications where outlier performance is critical.

Figure 7a shows the MAE values, averaged from regions 1, 2 and 3, vs. the scale factor, s. Each colour (blue, red, green) refers to the simulation's start, middle and end, respectively, according to the analysis shown in Section III A. The MAE remains small for  $s \le 20$  but significantly increases for s > 20, especially for the highly turbulent field near the end of the simulation. The same behaviour is obtained for the RMSE lines in Fig. 7b. It is also shown that  $R^2 > 0.85$  for  $s \le 50$  is evidence of good statistical accuracy. Of significance is the fact that  $R^2 > 0.8$  for the green line (that is, the end-time temperature values) and  $R^2 > 0.75$  for the red line (i.e., the middletime temperature values) even when an ultra-low resolution image (s = 100) is being processed. The trend for the MAPE line is similar to that of MAE and RMSE, with a larger error deviation occurring near the end of the simulation (i.e., the green-filled region), where deviations in the reconstructed relative to the original temperature map become more apparent (Fig. 7d).

Figure 7e presents the behavior of the  $L_2$ -norm. As the blur scale increases, the  $L_2$ -norm tends to grow, reflecting the cumulative error introduced by the degradation in image quality. Like the RMSE, it captures the overall reconstruction performance with greater sensitivity to larger errors due to its quadratic nature. As the scale increases, the LR fields contain fewer fine details, making it progressively more challenging for DELFI to accurately reconstruct high-frequency components of the original profile. This loss of detail leads to an increase in the  $L_{\infty}$ -norm (Fig. 7f), which here serves as an effective indicator of the worst-case performance of the SR

PLEASE CITE THIS ARTICLE AS DOI: 10.1063/5.0250478

Preprint

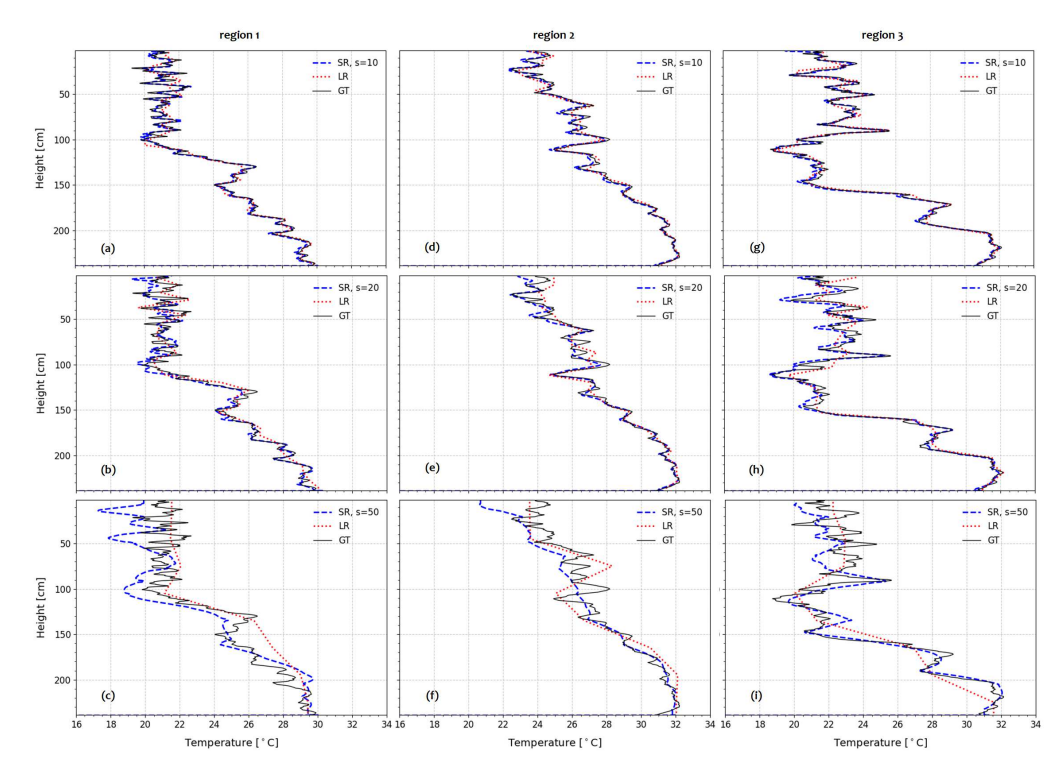


FIG. 6. Temperature profiles taken near the end of the simulation. The SR-extracted are compared to the ground truth (GT) profiles for region 1 and resolution (a) s=10, (b) s=20, and (c) s=50, for region 2 and (d) s=10, (e) s=20, and (f) s=50, for region 3 and (g) s=10, (h) s=20, and (i) s=50. Red dotted lines are the respective LR inputs used for training.

model.

# C. Discussion

Deep learning methods for turbulent flow reconstruction are employed to extract the temperature map of an indoor region. These methods function synergistically with computational fluid dynamics simulations. The simulation-extracted temperature fields are exploited to train the SR model.

After passing through DELFI, the reconstructed fields resemble the GT counterparts, although some smoothing appears. This is a common outcome in most SR models, where the features that appear to be missing in the model's output are predominantly small-scale details that, while visually distinct, may not significantly influence the key metrics in the target application. This fact, however, does not necessarily mean the model fails to enhance the LR image; instead, it suggests that the enhancement is focused on reconstructing the most critical aspects of the flow field, which are often the features of most

significant practical importance.

The next crucial step, of practical importance, is to incorporate the trained model to enhance authentic images captured by a camera within the room. In this direction, the model can provide high-resolution images, even if the camera images are of ultra-low resolution, scaled down to 50 times lower than the original. The results demonstrate the capacity of SR architectures to upscale low-level information into high-resolution practically and rapidly, effectively providing a close-to-the-ground truth field.

9

Furthermore, it has been shown that a single camera device can be used for data collection and analysis in similar situations where monitoring a specific quantity is required. This approach can replace a complex, specialized sensor array, offering a more cost-effective solution.

The next important step is to leverage the trained model to enhance images captured by a camera within the room. The model can significantly improve the quality of low-resolution camera images by generating high-resolution outputs up to 50 times larger than the original. These results underscore the

PLEASE CITE THIS ARTICLE AS DOI: 10.1063/5.0250478

Preprint 10

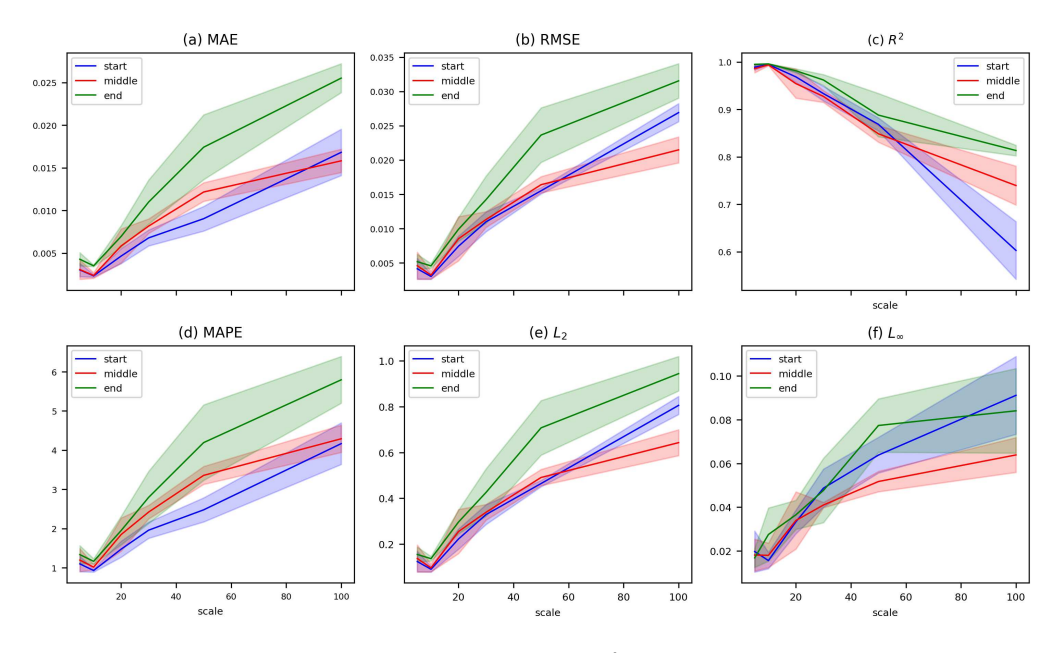


FIG. 7. Accuracy metrics for the reconstructed profiles. (a) MAE, (b) RMSE, (c)  $R^2$ , (d) MAPE, (e)  $L_2$ , and (f)  $L_\infty$ . The filled-coloured regions denote the property variation in regions 1, 2 and 3, while the lines correspond to the average values.

capacity of the model to provide accurate and practical SR, offering a cost-effective alternative to specialized sensor arrays for monitoring specific data.

Here, we also present temperature profiles across the room in regions where turbulent flow is observed, causing temperature values to vary widely in time and space. The reconstructed profiles are compared to the ground truth (i.e., the high-resolution simulation profiles). The quantitative error measures, such as the MAE, RMSE, MAPE,  $L_2$ , and  $L_\infty$  increase with lower input image resolution. However, they remain at satisfying levels even when the down-scaling approaches values of s=50-100. The coefficient of determination remains high even for  $s\leq 50$  ( $R^2>0.80$ ), showing good statistical accuracy during the reconstruction process.

For applications requiring highly detailed local features, the model's current behavior might necessitate further refinement. To improve the preservation of finer features, an advanced computational framework would include adversarial training (e.g., with GANs) or hybrid approaches that combine physical priors or constraints with DL to ensure that the reconstructed output adheres to known physical laws. Regarding the data acquisition setup, future advancements of this work will involve integrating the computational platform with a real thermal camera and a sensor array to assess the model's performance with actual data. We believe such implementations will offer viable solutions for smart buildings and more complex constructions. These technologies can be integrated into

initial designs, accurately monitoring several environmental parameters such as temperature, pressure, indoor air quality, and harmful particle concentration.

# IV. CONCLUSIONS

The study focused on reconstructing temperature profiles in a room using an SR model to enhance images from a single camera, aiming to replace complex sensor arrays. The research evaluates temperature profiles at three specific time points during a simulation: near the start, middle, and end. Three regions within the room experiencing the most turbulent airflow are analyzed.

Results demonstrate that the SR model can reliably reconstruct temperature profiles from low-resolution images across different regions, even with a 17-pixel height. Despite some inaccuracies in highly turbulent areas, the model's overall accuracy remains satisfactory, with outputs closely matching the ground truth, especially for downscaled images up to s=50.

Quantitative analyses using accuracy metrics indicated that errors increase with lower input image resolutions yet remain acceptable for  $s \leq 50$ . The findings suggest that the SR model offers a cost-effective alternative to sensor arrays by efficiently generating high-resolution temperature maps from low-resolution camera inputs.

The future direction includes integrating the model with

accepted manuscript. However, the online version of record will be different from this version once it has been copyedited and typeset This is the author's peer reviewed,

PLEASE CITE THIS ARTICLE AS DOI: 10.1063/5.0250478

Preprint 11

real thermal cameras and sensors to evaluate performance with actual data, aiming to develop viable solutions for monitoring environmental parameters in smart buildings and complex structures.

### **ACKNOWLEDGMENTS**

This paper is supported by the European Union's Horizon Europe Research and Innovation Actions programme under grant agreement No 101069937, project name HS4U (HEALTHY SHIP 4U). The views and opinions expressed are those of the author(s) only and do not necessarily reflect those of the European Union or the European Climate, Infrastructure, and Environment Executive Agency. Neither the European Union nor the granting authority can be held responsible for them.

### DATA AVAILABILITY

The data supporting this study's findings are available on request.

# REFERENCES

- <sup>1</sup>Y. Yasuda, R. Onishi, and K. Matsuda, "Super-resolution of three-dimensional temperature and velocity for building-resolving urban microm-eteorology using physics-guided convolutional neural networks with image inpainting techniques," Building and Environment 243, 110613 (2023).
- <sup>2</sup>F. Chi, L. Xu, J. Pan, R. Wang, Y. Tao, Y. Guo, and C. Peng, "Prediction of the total day-round thermal load for residential buildings at various scales based on weather forecast data," Applied Energy 280, 116002 (2020).
- <sup>3</sup>D. Lai, W. Liu, T. Gan, K. Liu, and Q. Chen, "A review of mitigating strategies to improve the thermal environment and thermal comfort in urban outdoor spaces," Science of The Total Environment 661, 337–353 (2019).
- <sup>4</sup>S. Vidas, P. Moghadam, and M. Bosse, "3d thermal mapping of building interiors using an rgb-d and thermal camera," in 2013 IEEE International Conference on Robotics and Automation (2013) pp. 2311–2318.
- 51. Zhu, Y. Xu, L. Hoegner, and U. Stilla, "Generation of thermal point clouds from uncalibrated thermal infrared image sequences and mobile laser scans," IEEE Transactions on Instrumentation and Measurement 72, 116 (2022).
- 6H. Xiao and P. Cinnella, "Quantification of model uncertainty in rans simulations: A review," Progress in Aerospace Sciences 108, 1–31 (2019).
- <sup>7</sup>R. D. Moser, S. W. Haering, and G. R. Yalla, "Statistical properties of subgrid-scale turbulence models," Annual Review of Fluid Mechanics 53, 255–286 (2021).
- <sup>8</sup>S. B. Pope, "Ten questions concerning the large-eddy simulation of turbulent flows," New Journal of Physics 6, 35 (2004).
- <sup>9</sup>C. A. Duque-Daza, J. Murillo-Rincón, A. S. Espinosa-Moreno, F. Alberini, A. Alexiadis, D. A. Garzón-Alvarado, A. M. Thomas, and M. J. Simmons, "Analysis of the airflow features and ventilation efficiency of an ultra-clean-air operating theatre by qdns simulations and experimental validation," Building and Environment 256, 111444 (2024).
- <sup>10</sup> High-resolution methods for incompressible and low-speed flows (Springer Science & Business Media, 2005).
- <sup>11</sup> J. Ling, A. Kurzawski, and J. Templeton, "Reynolds averaged turbulence modelling using deep neural networks with embedded invariance," Journal of Fluid Mechanics 807, 155–166 (2016).

<sup>12</sup>J. Y. Park and Z. Nagy, "Comprehensive analysis of the relationship between thermal comfort and building control research - a data-driven literature review," Renewable and Sustainable Energy Reviews 82, 2664–2679 (2018).

- <sup>13</sup>N. Somu, A. Sriram, A. Kowli, and K. Ramamritham, "A hybrid deep transfer learning strategy for thermal comfort prediction in buildings," Building and Environment 204, 108133 (2021).
- <sup>14</sup>A. Drakou, F. Sofos, T. E. Karakasidis, and A. Tsangrassoulis, "Adaptive thermal comfort model and active occupant behaviour in a mixed-mode apartment. a synergy to sustainability." IOP Conference Series: Earth and Environmental Science 1196, 012097 (2023).
- <sup>15</sup>G. Koppe, A. Meyer-Lindenberg, and D. Durstewitz, "Deep learning for small and big data in psychiatry," Neuropsychopharmacology 46, 176–190 (2021).
- <sup>16</sup>M. Lino, S. Fotiadis, A. A. Bharath, and C. D. Cantwell, "Current and emerging deep-learning methods for the simulation of fluid dynamics," Proceedings of the Royal Society A: Mathematical, Physical and Engineering Sciences 479, 20230058 (2023).
- <sup>17</sup>O. Obiols-Sales, A. Vishnu, N. Malaya, and A. Chandramowliswharan, "Cfdnet: a deep learning-based accelerator for fluid simulations," in *Proceedings of the 34th ACM International Conference on Supercomputing*, ICS '20 (Association for Computing Machinery, New York, NY, USA, 2020).
- <sup>18</sup>Y. Zhao, H. D. Akolekar, J. Weatheritt, V. Michelassi, and R. D. Sandberg, "Rans turbulence model development using cfd-driven machine learning," Journal of Computational Physics 411, 109413 (2020).
- <sup>19</sup>M. Bode and J. H. Göbbert, "Acceleration of complex high-performance computing ensemble simulations with super-resolution-based subfilter models," Computers & Fluids 271, 106150 (2024).
- <sup>20</sup>A. Kashefi, D. Rempe, and L. J. Guibas, "A point-cloud deep learning framework for prediction of fluid flow fields on irregular geometries," Physics of Fluids 33, 027104 (2021).
- <sup>21</sup>F. Sofos, D. Drikakis, I. W. Kokkinakis, and S. M. Spottswood, "A deep learning super-resolution model for turbulent image upscaling and its application to shock wave-boundary layer interaction," Physics of Fluids 36, 025117 (2024).
- <sup>22</sup>F. Sofos, G. Sofiadis, E. Chatzoglou, A. Palasis, T. Karakasidis, and A. Liakopoulos, "From sparse to dense representations in open channel flow images with convolutional neural networks." Inventions 9, 27 (2024).
- ages with convolutional neural networks," Inventions 9, 27 (2024).

  23 Y. LeCun, Y. Bengio, and G. Hinton, "Deep learning," Nature 521, 436-444 (2015).
- <sup>24</sup>G. Calzolari and W. Liu, "Deep learning to replace, improve, or aid cfd analysis in built environment applications: A review," Building and Enviropped 108 (1083) (2021).
- <sup>25</sup>M. Z. Yousif, L. Yu, S. Hoyas, R. Vinuesa, and H. Lim, "A deep-learning approach for reconstructing 3D turbulent flows from 2D observation data," Scientific Reports 13, 2529 (2023), publisher: Nature Publishing Group UK London
- 26J. N. Kutz, "Deep learning in fluid dynamics," Journal of Fluid Mechanics 814, 1–4 (2017).
- <sup>27</sup>K. Fukami, K. Fukagata, and K. Taira, "Super-resolution analysis via machine learning: a survey for fluid flows," Theoretical and Computational Fluid Dynamics 37, 421–444 (2023).
- <sup>28</sup>B. Liu, J. Tang, H. Huang, and X.-Y. Lu, "Deep learning methods for superresolution reconstruction of turbulent flows," Physics of Fluids 32, 025105 (2020).
- <sup>29</sup>J. Zheng, Y. Liu, Y. Feng, H. Xu, and M. Zhang, "Contrastive attention-guided multi-level feature registration for reference-based superresolution," ACM Transactions on Multimedia Computing, Communications, and Applications 20, Article 55, 21 pages (2023).
- <sup>30</sup>A. M. Collins, P. Rivera-Casillas, S. Dutta, O. M. Cecil, A. C. Trautz, and M. W. Farthing, "Super-resolution and uncertainty estimation from sparse sensors of dynamical physical systems," Frontiers in Water 5 (2023), 10 3389/frva 2023, 1137110
- <sup>31</sup>Z. Luo, L. Wang, J. Xu, M. Chen, J. Yuan, and A. C. C. Tan, "Flow reconstruction from sparse sensors based on reduced-order autoencoder state estimation." Physics of Fluids 35, 075127 (2023).
- <sup>32</sup>Y. Sha, Y. Xu, Y. Wei, and C. Wang, "Prediction of pressure fields on cavitation hydrofoil based on improved compressed sensing technology," Physics of Fluids 36, 013321 (2024).

PLEASE CITE THIS ARTICLE AS DOI: 10.1063/5.0250478

Preprint 12

<sup>33</sup> K. Manohar, B. W. Brunton, J. N. Kutz, and S. L. Brunton, "Data-driven sparse sensor placement for reconstruction: Demonstrating the benefits of exploiting known patterns," IEEE Control Systems Magazine 38, 63–86 (2018).

- <sup>34</sup>J. E. Santos, Z. R. Fox, A. Mohan, D. O'Malley, H. Viswanathan, and N. Lubbers, "Development of the Senseiver for efficient field reconstruction from sparse observations," Nature Machine Intelligence 5, 1317–1325 (2023).
- <sup>35</sup>Z. Li, J. Guo, Y. Zhang, J. Li, and Y. Wu, "Reference-based multi-level features fusion deblurring network for optical remote sensing images," Remote Sensing 14, 2520 (2022).
- <sup>36</sup>C. Szegedy, W. Liu, Y. Jia, P. Sermanet, S. Reed, D. Anguelov, D. Erhan, V. Vanhoucke, and A. Rabinovich, "Going deeper with convolutions," in 2015 IEEE Conference on Computer Vision and Pattern Recognition (CVPR) (2015) pp. 1–9.
- <sup>37</sup>G. Zaid, L. Bossuet, A. Habrard, and A. Venelli, "Methodology for efficient cnn architectures in profiling attacks," IACR Transactions on Cryptographic Hardware and Embedded Systems 2020, 1–36 (2019).
- <sup>38</sup>A. Khan, A. Sohail, U. Zahoora, and A. S. Qureshi, "A survey of the recent architectures of deep convolutional neural networks," Artificial Intelligence Review 53, 5455–5516 (2020).
- <sup>39</sup>R. F. Cerqueira and E. E. Paladino, "Development of a deep learning-based image processing technique for bubble pattern recognition and shape reconstruction in dense bubbly flows," Chemical Engineering Science 230, 116163 (2021).
- <sup>40</sup>M. Morimoto, K. Fukami, K. Zhang, A. G. Nair, and K. Fukagata, "Convolutional neural networks for fluid flow analysis: toward effective metamodeling and low dimensionalization," Theoretical and Computational Fluid Dynamics 35, 633–658 (2021).
- <sup>41</sup>F. Sofos, D. Drikakis, I. W. Kokkinakis, and S. M. Spottswood, "Convolutional neural networks for compressible turbulent flow reconstruction," Physics of Fluids 35, 116120 (2023).
- <sup>42</sup>O. Ronneberger, P. Fischer, and T. Brox, "U-net: Convolutional networks for biomedical image segmentation," in *Medical Image Computing and Computer-Assisted Intervention MICCAI 2015*, edited by N. Navab, J. Hornegger, W. M. Wells, and A. F. Frangi (Springer International Publishing, Cham, 2015) pp. 234–241.
- <sup>43</sup>K. He, X. Zhang, S. Ren, and J. Sun, "Deep residual learning for image recognition," in 2016 IEEE Conference on Computer Vision and Pattern Recognition (CVPR) (2016) pp. 770–778.
- <sup>44</sup>C. Kong, J.-T. Chang, Y.-F. Li, and R.-Y. Chen, "Deep learning methods for super-resolution reconstruction of temperature fields in a supersonic combustor," AIP Advances 10, 115021 (2020).
- <sup>45</sup>X.-L. Zhang, H. Xiao, G.-W. He, and S.-Z. Wang, "Assimilation of disparate data for enhanced reconstruction of turbulent mean flows," Computers & Fluids 224, 104962 (2021).
- <sup>46</sup>G. Allaire, S. Clerc, and S. Kokh, "A five-equation model for the simulation of interfaces between compressible fluids," Journal of Computational Physics 181, 577–616 (2002).
- <sup>47</sup> A. W. Cook, "Enthalpy diffusion in multicomponent flows," Physics of Fluids 21, 055109 (2009).
- <sup>48</sup>D. Drikakis and S. Tsangaris, "On the solution of the compressible navier-stokes equations using improved flux vector splitting methods," Applied Mathematical Modelling 17, 282–297 (1993).
- <sup>49</sup>A. Bagabir and D. Drikakis, "Numerical experiments using high-resolution schemes for unsteady, inviscid, compressible flows," Computer Methods in Applied Mechanics and Engineering 193, 4675–4705 (2004).
- <sup>50</sup>I. W. Kokkinakis, D. Drikakis, K. Ritos, and S. M. Spottswood, "Direct numerical simulation of supersonic flow and acoustics over a compression

- ramp," Physics of Fluids 32, 066107 (2020).
- <sup>51</sup>D. Drikakis, M. Hahn, A. Mosedale, and B. Thornber, "Large eddy simulation using high-resolution and high-order methods," Philosophical Transactions of the Royal Society A: Mathematical, Physical and Engineering Sciences 367, 2985–2997 (2009).
- <sup>52</sup>D. Drikakis and P. K. Smolarkiewicz, "On spurious vortical structures," Journal of Computational Physics 172, 309–325 (2001).
- <sup>53</sup>A. F. Antoniadis, P. Tsoutsanis, and D. Drikakis, "Assessment of high-order finite volume methods on unstructured meshes for rans solutions of aeronautical configurations," Computers & Fluids 146, 86–104 (2017).
- <sup>54</sup>F. Grinstein, L. Margolin, and W. Rider, "Implicit large eddy simulation: Computing turbulent fluid dynamics," Implicit Large Eddy Simulation: Computing Turbulent Fluid Dynamics (2007), 10.1017/CBO9780511618604.
- <sup>55</sup>D. Drikakis, C. Fureby, F. Grinstein, and D. Youngs, "Simulation of transition and turbulence decay in the taylor–green vortex," Journal of Turbulence 8 (2007), 10.1080/14685240701250289.
- <sup>56</sup>M. Hahn and D. Drikakis, "Large eddy simulation of compressible turbulence using high-resolution methods," International Journal for Numerical Methods in Fluids 47, 971–977 (2005), https://onlinelibrary.wiley.com/doi/pdf/10.1002/fld.882.
- <sup>57</sup>A. Mosedale and D. Drikakis, "Assessment of very high order of accuracy in implicit les models," Journal of Fluids Engineering 129, 1497–1503 (2007), https://asmedigitalcollection.asme.org/fluidsengineering/articlepdf/129/12/1497/5729131/1497\_1-pdf.
- <sup>58</sup>E. F. Toro, Riemann Solvers and Numerical Methods for Fluid Dynamics, A Practical Introduction, 3rd ed. (Springer-Verlag Berlin Heidelberg, 2009).
- <sup>59</sup>I. Kokkinakis and D. Drikakis, "Implicit large eddy simulation of weakly-compressible turbulent channel flow," Computer Methods in Applied Mechanics and Engineering 287, 229 261 (2015).
   <sup>60</sup>B. J. R. Thornber and D. Drikakis, "Numerical dissipation
- 60B. J. R. Thornber and D. Drikakis, "Numerical dissipation of upwind schemes in low mach flow," International Journal for Numerical Methods in Fluids 56, 1535–1541 (2008), https://onlinelibrary.wiley.com/doi/pdf/10.1002/fld.1628.
- <sup>61</sup>I. Kokkinakis, D. Drikakis, D. Youngs, and R. Williams, "Two-equation and multi-fluid turbulence models for rayleigh-taylor mixing," International Journal of Heat and Fluid Flow 56, 233–250 (2015).
- <sup>62</sup>I. W. Kokkinakis, D. Drikakis, and D. L. Youngs, "Vortex morphology in richtmyer-meshkov-induced turbulent mixing," Physica D: Nonlinear Phe-1071 12345 (2020).
- <sup>63</sup>C. Bogey and C. Bailly, "Computation of a high Reynolds number jet and its radiated noise using large eddy simulation based on explicit filtering,"
- <sup>64</sup>S. Albawi, T. A. Mohammed, and S. Al-Zawi, "Understanding of a convolutional neural network," in 2017 International Conference on Engineering and Technology (ICET) (2017) pp. 1–6.
- 65 J. Kim, J. K. Lee, and K. M. Lee, "Accurate image super-resolution using very deep convolutional networks," in 2016 IEEE Conference on Computer Vision and Pattern Recognition (CVPR) (2016) pp. 1646–1654.
- <sup>66</sup>T. Falk, D. Mai, R. Bensch, O. Cicek, A. Abdulkadir, Y. Marrakchi, A. Bohm, J. Deubner, Z. Jackel, K. Seiwald, A. Dovzhenko, O. Tietz, C. Dal Bosco, S. Walsh, D. Saltukoglu, T. L. Tay, M. Prinz, K. Palme, M. Simons, I. Diester, T. Brox, and O. Ronneberger, "U-Net: deep learning for cell counting, detection, and morphometry," Nature Methods 16, 67–70
- <sup>67</sup>H. Tajbakhsh, Z. Abadin, and P. M. Ferreira, "L<sub>∞</sub> parameter estimates for volumetric error in models of machine tools," Precision Engineering 20, 179–187 (1997).